APPENDIX I: ACCEPTANCE OF THE 8 GEV SPECTROMETER

The solid-angle acceptance of the 8 GeV Spectrometer was calculated in two primary steps that utilized the SLAC beam transport program TRANSPORT[81] and a Monte-Carlo ray-tracing program initiated by C. Jordan.[82] Prior to these calculations, a computer model of the spectrometer was formulated; it incorporated ideal dipole and quadrupole magnet elements as well as drift spaces and apertures. The program TRANSPORT used this model to generate matrices of transport coefficients that describe the passage of charged particles through the spectrometer magnet array. The transport coefficients are first-and second-order coefficients in a Taylor series expansion of the particle coordinates $(x,\theta,y,\phi,z,\delta = \Delta P/P)$ about the spectrometer central ray. In the second step the matrices of transport coefficients were used in the Monte Carlo program to calculate the acceptance of the individual segments of the spectrometer focal planes.

The TRANSPORT model of the 8 GeV Spectrometer, the same for all momenta, is listed in Table (XXII) for P = 8.0051 GeV/c. Negative quadrupole fields indicate vertical focussing; ψ is the pole-face rotation of the bending magnets relative to the central ray. Similar models, with only the magnet field strengths altered, were used at P = 3.0062, 6.0091, and 9.0026 GeV/c, where optics data on the 8 GeV Spectrometer were available.[83] Table (XXIII) lists the magnet field strengths used at these

Table XXII. TRANSPORT model of the 8 GeV spectrometer

P = 8.0051 GeV/c

1. drift from target: 2.295 m
2. quadrupole Q81 (z = 1.034 m, a = 13.97 cm, 7.488 kg)
3. drift: 0.352 m
4. aperture #1 (circle: $(x^2 + (y + .24)^2)^{1/2} < 13.02$ cm)
5. drift: 0.614 m
6. quadrupole Q82 (z = 1.334 m, a = 19.37 cm, -10.827 kg)
7. drift: 0.962 m
8. 1/2 of dipole B81 (z = 1.8135 m, $\psi = 7.5^{\circ}$, 19.274 kg, n = 0)
9. aperture (-19.21 cm <y< 34.47 cm)
10. 1/2 of dipole B81 (z = 1.8135 m, $\psi = 7.5^{\circ}$, 19.274 kg, n = 0)
11. drift: 0.3863 m
12. swing mask (normally out)
13. drift: 0.5387 m
14. dipole B82 (z = 3.627 m, $\psi = 7.5^{\circ}$, 19.274 kg, n = 0)
15. drift: 0.762 m
16. aperture #2 (octagon: $|y| < 16.5$ cm, $|x| < 14.5$ cm, and $|y| < (24.6 \text{ cm})\left(1 - \frac{|x|}{18.2 \text{ cm}}\right)$)
17. drift: 0.243 m
18. quadrupole Q83 (z = 1.334 m, a = 19.37 cm, -7.332 kg)
19. drift: 4.198 m
20. theta focal plane
21. drift: 0.555 m
22. momentum focal plane

total path length z_{tot} = 21.861 m

Table XXIII. Magnet field strengths used in TRANSPORT

Magnet	P = 3.0062	P = 6.0091	P = 8.0051	P = 9.0026
Q81	2.788 (-2.1)	5.620 (-1.3)	7.488 (-1.3)	8.365 (-2.0)
Q82	-4.013 (2.0)	-8.116 (0.8)	-10.827 (0.6)	-11.986 (2.0)
B81	7.238 (0.0)	14.468 (0.0)	19.274 (0.0)	21.675 (0.0)
B82	7.238 (0.0)	14.468 (0.0)	19.274 (0.0)	21.675 (0.0)
Q83	-2.703 (-0.7)	-5.442 (-1.4)	-7.332 (-2.4)	-8.428 (-4.7)

(units are kg)

(quadrupole fields are given at pole tip)

momenta; the numbers in parentheses represent the percentage deviation from the measured field strengths[83], assuming linearity. The reason for the deviations in the quadrupole strengths is discussed in the following paragraph.

The principal first-order transport coefficients measured in the optics tests are listed in Table (XXIV); their estimated accuracy is 1%.[83] When the measured magnet field strengths were used in the above TRANSPORT model, we could not reproduce these measured coefficients. We felt that these discrepancies were caused by the proximity of the magnets to the steel frame of the spectrometer and to each other, resulting in distortion of their fringing fields.[83] In addition, the field strengths and effective magnet lengths were not known better than 1%. Consequently, we made an extensive study of TRANSPORT models, in which several of the available parameters (e.g., field strengths and pole-face rotations) were varied in different combinations until a selected set of transport coefficients agreed with the measured values. We hoped we could simulate the non-ideal behavior and better approximate the measured transport coefficients with such an adjusted TRANSPORT model. The final TRANSPORT model chosen had varied the three quadrupole field strengths so that $\langle x|x_o\rangle$, $\langle x|\theta_o\rangle$, and $\langle y|\delta_o\rangle$ (where the subscript $_o$ denotes values at the target) reproduced the measured values. The best-fit values

Table XXIV. Measured transport coefficients

Coefficient	P = 3.0062	P = 6.0091	P = 8.0051	P = 9.0026
$\langle x \mid x_o \rangle$	0.0385	0.0206	0.0277	0.0153
$\langle x \mid \theta_o \rangle$	4.5170	4.5468	4.5750	4.5902
$\langle \theta \mid x_o \rangle$	-0.1868	-0.2157	-0.1936	-0.2043
$\langle \theta \mid \theta_o \rangle$	4.7907	4.8245	4.8576	4.8805
$\langle y \mid \phi_o \rangle$	0.0007	-0.0014	-0.0041	-0.0047
$\langle y \mid \delta_o \rangle$	-2.9591	-2.9389	-2.9067	-2.8439
$\langle \phi \mid \phi_o \rangle$	-1.0740	-1.0757	-1.0769	-1.0787
$\langle \phi \mid \delta_o \rangle$	0.0789	0.0857	0.0935	0.1130

(lengths are in cm; angles in mrad; δ in percent)

of the quadrupole field strengths are those listed in Table (XXIII).

The criterion for an acceptable TRANSPORT model was that it reproduce solid angle maps measured in the optics tests[29]. Solid-angle maps were generated from each model using a ray-tracing program developed by E. Taylor[84]; they were then compared with the measured maps. All TRANSPORT models examined were capable of reproducing some subset of the measured transport coefficients; these were usually chosen to include the two dispersions $\langle x|\theta_o\rangle$ and $\langle y|\delta_o\rangle$, as they directly influence the acceptance. But the various models predicted fairly different results for the solid-angle maps and could be distinguished by this criterion. Comparisons of solid-angle maps were attempted only at P = 8 GeV; the choice of TRANSPORT model was assumed independent of momentum. We ascertained that the model that best approximated the measured solid-angle maps was the model used in all previous calculations[41, 85] of the 8 GeV acceptance: the field strengths of Q81, Q82, and Q83 were varied independently to fit the transport coefficients $\langle x|x_o\rangle$, $\langle x|\theta_o\rangle$, and $\langle y|\delta_o\rangle$. Table (XXV) lists the principal first-order transport coefficients as obtained using this canonical TRANSPORT model at P = 3.0, 6.0, 8.0, and 9.0 GeV/c; these coefficients should be compared with the measured values from Table (XXIV).

A Monte-Carlo program used matrices of transport coefficients to calculate the solid-angle acceptance $\Delta\theta\Delta\phi\Delta P/P$ of the 8 GeV

Table XXV. Transport coefficients from the TRANSPORT model

Coefficient	P = 3.0062	P = 6.0091	P = 8.0051	P = 9.0026
$\langle x \mid x_o \rangle$*	0.0385	0.0206	0.0277	0.0153
$\langle x \mid \theta_o \rangle$*	4.5170	4.5468	4.5750	4.5902
$\langle \theta \mid x_o \rangle$	-0.1805	-0.1980	-0.1889	-0.2014
$\langle \theta \mid \theta_o \rangle$	4.8004	4.8449	4.8942	4.9459
$\langle y \mid \phi_o \rangle$	0.0066	-0.0064	-0.0139	-0.0139
$\langle y \mid \delta_o \rangle$*	-2.9591	-2.9389	-2.9067	-2.8439
$\langle \phi \mid \phi_o \rangle$	-1.0900	-1.0830	-1.0921	-1.1375
$\langle \phi \mid \delta_o \rangle$	0.1106	0.1479	0.2074	0.3230

(lengths are in cm; angles in mrad; δ in percent)

*the values for this coefficient are equal to the measured values by definition.

Spectrometer. Acceptances were calculated for each P-θ bin, defined as the intersection of two adjacent θ-counters and two adjacent P-counters in the spectrometer focal planes; these acceptances were then summed to get the total acceptance. Scattered rays (x_o, θ_o, y_o, ϕ_o, z_o, δ_o) were generated randomly at the target position; for large N, they were distributed uniformly over a segment $\Delta\theta_o\ \Delta\phi_o\ \Delta\delta_o$ that completely overlapped the spectrometer acceptance. The initial volume $\Delta x_o\ \Delta y_o\ \Delta z_o$ reflected the target length and beam spot size. The rays were propagated through five successive segments of the spectrometer according to the transport coefficients for that segment. Each ray was required to clear 13 different apertures within the spectrometer or was rejected. Actually, only two lead apertures, one behind Q81 and the other behind B82, determined the solid-angle acceptance. For each P-θ bin, $\Delta\delta$ and $\Delta\theta$ were determined solely by the edges of the counters themselves; $\Delta\delta$ and $\Delta\theta$ were therefore directly related to the measured dispersions $\langle x|\theta_o\rangle$ and $\langle y|\delta_o\rangle$. The $\Delta\phi$ for each P-θ bin was determined by the lead apertures behind Q81 and B82. The acceptance $(\Delta\theta\Delta\phi\Delta\delta)_{ij}$ of the i-jth P-θ bin was taken to be

$$(\Delta\theta\Delta\phi\Delta\delta)_{ij} = \frac{N_{ij}}{N}(\Delta\theta_o\Delta\phi_o\Delta\delta_o) \qquad (A.1.1)$$

where N_{ij} is the number of events falling into this bin and N is the total number of Monte-Carlo events.

Three-dimensional computer models of the P- and θ-hodoscopes

permitted a more accurate calculation of acceptances. Each hodoscope was modelled by two parallel, segmented planes that represented the two rows of scintillation counters. Monte Carlo events were binned at each focal plane according to the segments (read counters) of the two planes through which the event passed. In this way "shadowing" effects, which arose from the non-zero divergence and convergence of scattered rays at the focal planes, were adequately simulated. This more faithful representation of the hodoscopes allowed a much more accurate calculation of the acceptances of each P-θ bin. These shadowing effects were quite severe ($\sim$20%) for a single bin. Errors of about 1% in the total acceptance resulted if one did not account for these effects. Consequently, this three-dimensional computer model of the hodoscopes is felt to be the primary advantage of the present acceptance calculation.

Monte Carlo acceptance calculations were made at P = 3.0, 6.0, 8.0, and 9.0 GeV/c using the TRANSPORT model of Table ($XXII$) with the appropriate magnet field strengths from Table ($XXIII$). Samples of 4×10^5 Monte Carlo events were used, insuring that 100-500 events fell into each of the 20 x 54 P-θ bins. The acceptances of the individual bins were somewhat inaccurate statistically, but the total acceptance was well known. The results of these calculations are shown in Table ($XXVI$) for two definitions of the spectrometer acceptance. ACCP2 is the nominal

Table XXVI. Acceptance of the 8 GeV spectrometer

P (GeV/c)	ACCP1 (x 10^{-3}msr)	ACCP2 (x 10^{-3}msr)	Δ (%)
3.0062	27.01	24.69	-0.92
6.0091	27.37	24.89	-0.12
8.0051	27.32	24.95	+0.12
9.0026	26.76	24.69	-0.92
Average	27.35	24.92	

acceptance definition used in experiment A; it includes only P-bins 2-19 and θ-bins 2-53. The optics measurements at 3 GeV/c were somewhat in doubt due to the effects of multiple scattering[83], and we felt that saturation might be setting in at 9 GeV/c. Consequently the acceptance for experiment A was taken to be the average of ACCP2 from the 6 and 8 Gev/c calculations. Δ is the percentage difference of ACCP2 from the average value. No significance is attached to the P-dependence of the acceptance evident in Table (XXVI). Calculations with different TRANSPORT models, which simulated the solid-angle maps almost as well, showed different momentum dependences. We only conclude that the possible error due to momentum dependence of the acceptance is about $\pm$ 1.0%.

Tests of the solid-angle acceptance of the 8 GeV Spectrometer were made using the tungsten slits in front of the spectrometer entrance window, before the first quadrupole magnet Q81. The vertically opening φ-slits can determine $\Delta\phi_{ij}$ independent of the apertures within the spectrometer. As $\Delta\theta_{ij}$ and $\Delta\delta_{ij}$ were already well-known from the optics measurements, the φ-slits allowed an accurate check of the TRANSPORT model calculations. The solid-angle acceptance was calculated by the Monte Carlo program for six different settings of the φ-slits ranging from fully open to $\Delta\phi$ = 13 mrad, where $\Delta\phi_{ij}$ was almost completely determined by the tungsten slits.

Experimental runs of $\sim 10^4$ counts at each of these slit settings revealed that (yield/acceptance) was constant within 1%. It was important to correct for $\Delta\phi$ shifts in the effective scattering angle in these calculations, as this effect was about 1% itself. Based upon the results of this solid-angle test and on the quoted 1% accuracy[83] of the optics measurements, we conclude that the acceptance of the 8 GeV Spectrometer is accurate to 1.5% and the momentum dependence accurate to $\pm$ 1.0%.

APPENDIX II: RADIATIVE CORRECTION FORMULAE

We give here the formulae used to radiatively correct the elastic and inelastic cross sections. Discussion of these equations and their application to the data may be found in section VI.

The radiative tail $I_1(E_o,E',\theta,t)$ from elastic e-p scattering was determined from an expression derived by Friedman.[86]

$$I_1(E_o,E',\theta,t) = I_1^B + I_1^A \qquad \text{(A.II.1)}$$

where

$$I_1^B = [1 + 0.58b(\ell_A+\ell_B)][(\ln\frac{E_{of}}{E'})^{b\ell_A}(\ln\frac{E_o}{E_c})^{b\ell_B}$$

$$\cdot \{\frac{bt_AR_A}{E_{of}-E'}\sigma(E_o) + v'X(E_o,E',\theta)\frac{P_A}{P_A+P_B}\}aC_A]$$

$$I_1^A = [1 + 0.58b(\ell_A+\ell_B)][(\ln\frac{E_o}{E_o'})^{b\ell_B}(\ln\frac{E_c'}{E'})^{b\ell_A}$$

$$\cdot \{\frac{bt_BR_B}{E_o-E_o'}\frac{\sigma(E_o')}{(1-\frac{2E'}{M}\sin^2\frac{\theta}{2})^2} + v'X(E_o,E',\theta)\frac{P_B}{P_A+P_B}\}\beta C_B].$$

$$v' = 1 + (v_A + v_B)(\tfrac{1}{2} + \tfrac{1}{2}\ln\eta)$$

$$P_A = S_A\,\sigma(E_o)/(E_{of}-E')$$

$$P_B = S_B\,\sigma(E_o')/(E_o-E_o')(1-\frac{2E'}{M}\sin^2\frac{\theta}{2})^2$$

$$S_A = \frac{E'}{E_{of}} + \frac{1}{2}(\frac{E_{of}-E'}{E_{of}})^2$$

$$S_B = \frac{E_o'}{E_o} + \frac{1}{2}(\frac{E_o-E_o'}{E_o})^2.$$

$$R_A = \left[\frac{E'}{E_{of}} + \frac{3}{4}\left(\frac{E_{of}-E'}{E_{of}}\right)^2\right]$$

$$R_B = \left[\frac{E'_o}{E_o} + \frac{3}{4}\left(\frac{E_o-E'_o}{E_o}\right)^2\right]$$

$$a = \frac{1}{\left(\ln\frac{E_o}{E_c}\right)^{b\ell_B}}\left[\left(\ln\frac{E_o}{E_o-0.10k}\right)^{b\ell_B} + b\ell_B\left(\ln\frac{E_o}{E_o-0.20k}\right)^{b\ell_B}\frac{\sigma(E_o-0.20k)}{\sigma(E_o)}\right.$$

$$+ \frac{2}{3}b\ell_B\left(\ln\frac{E_o}{E_o-0.45k}\right)^{b\ell_B}\frac{\sigma(E_o-0.45k)}{\sigma(E_o)}$$

$$\left. + \frac{1}{2}b\ell_B\left(\ln\frac{E_o}{E_o-0.80k}\right)^{b\ell_B}\frac{\sigma(E_o-0.80k)}{\sigma(E_o)}\right]$$

$$\beta = \frac{1}{\left(\ln\frac{E'_c}{E'}\right)^{b\ell_A}}\left[\left(\ln\frac{E'+0.10\rho}{E'}\right)^{b\ell_A} + b\ell_A\left(\ln\frac{E'+0.20\rho}{E'}\right)^{b\ell_A}\frac{\sigma(E'_o+0.20k)}{\sigma(E'_o)}\right.$$

$$+ \frac{2}{3}b\ell_A\left(\ln\frac{E'+0.45\rho}{E'}\right)^{b\ell_A}\frac{(E'_o+0.45k)}{\sigma(E'_o)}$$

$$\left. + \frac{1}{2}b\ell_A\left(\ln\frac{E'+0.80\rho}{E'}\right)^{b\ell_A}\frac{\sigma(E'_o+0.80k)}{\sigma(E'_o)}\right]$$

$$\rho = E'_c - E'; \quad k = \frac{E_o - E'_o}{2}; \quad E_c = \frac{E_o + E'_o}{2}$$

$$C_A(\ell_A,E',E_{of}) = \{1 + b\ell_A\,[-0.733229 + 1.0783\,(\frac{E'}{E_{of}})$$

$$+ 0.349814\,(\frac{E'}{E_{of}})^2 - 0.636089\,(\frac{E'}{E_{of}})^3\,]\}$$

$$\cdot\ \{\frac{1.045(0.99 - \frac{E'}{E_{of}})}{0.89} + \frac{0.962(\frac{E'}{E_{of}} - 0.010)}{0.89}\}$$

$$C_B(\ell_B,E'_o,E_o) = C_A(\ell_B,E'_o,E_o)$$

C_A and C_B were empirical corrections[87] for approximations made in the solution of the diffusion equation for the straggling functions.

$X(E_o,E',\theta)$ is the exact tail from internal bremsstrahlung calculated to lowest order in α according to Mo and Tsai.[43, 44]

$$\ell_A = t_A + v_A/b$$

$$\ell_B = t_B + v_B/b$$

t_B and t_A are the radiation lengths before and after scattering discussed in section VI.B.

$$v_A = v_B = \frac{\alpha}{\pi}\,(\ln\frac{q^2}{m^2} - 1)$$

$$b = \frac{4}{3}$$

m = the electron mass

$$E_{of} = E_o/(1 + \frac{2E_o}{M} \sin^2(\frac{\theta}{2}))$$

$$E'_o = E'/(1 - \frac{2E'}{M} \sin^2(\frac{\theta}{2}))$$

$$E'_c = E_c/(1 + \frac{2E_c}{M} \sin^2(\frac{\theta}{2}))$$

$\sigma(E_o)$ is the elastic-scattering cross section calculated according to the Rosenbluth equation.[88]

$$\sigma(E_o,\theta) = \frac{\alpha^2}{4E_o^2} (\frac{\cos^2\theta/2}{\sin^4\theta/2}) (\frac{1}{1 + (\frac{2E_o}{M})\sin^2\theta/2})$$

$$\cdot \{(\frac{G_E^2 + \tau G_M^2}{1 + \tau} + 2\tau G_M^2 \tan^2\frac{\theta}{2}\}$$

where $\tau = Q^2/4M^2$.

$$G_E = \frac{1}{\mu_p} G_M = f_M(Q) \ (1 + Q^2/0.71)^{-2}$$

The function $f_M(Q)$ is a modulating factor that varies about the value of 1.0. It is from a fit by Miller[41] to all previous SLAC elastic e-p data.[29, 40]

$$f_M(Q) = \sum_{i=0}^{i=5} a_i \prod_{j=0}^{j=5} \frac{(Q - Q_j)}{(Q_i - Q_j)} \qquad \text{(A.II.2)}$$

where $Q = \sqrt{Q^2}$, and the coefficients a_i are equal to the value of the function $f(Q)$ at $Q = i$.

$$a_0 = 1.000$$

$$a_1 = 1.018$$

$$a_2 = 1.056$$

$$a_3 = 0.836$$

$$a_4 = 0.687$$

$$a_5 = 0.673$$

The quasi-elastic and elastic tails calculated in the equivalent radiator approach were from an expression derived by Sogard.[89] They were calculated for proton, neutron, and deuteron (see Section IV.D.4) according to

$$I_1^{ER}(E_o, E', \theta, t) = \tag{A.II.3}$$

$$\frac{(1+a)^{b'(\ell_A+\ell_B)}}{\Gamma(1+b'\ell_A)\,\Gamma(1+b'\ell_B)} e^{-b'[\ell_B \ln(E_o/\Delta)+\ell_A \ln(E'/\Delta)]} \frac{d^2\sigma}{d\Omega dE'}(E_o,E',\theta)_{TH}$$

$$+ \frac{(1+a)^{b'\ell_A}}{\Gamma(1+b'\ell_A)} e^{-b'\ell_A \ln(E'/\Delta)} \int_{E_{o_{min}}}^{E_o-\Delta} dE_o' \; \frac{d^2\sigma}{d\Omega dE'}(E_o',E',\theta)_{TH} I_e(E_o,E_o',\ell_B)$$

$$+ \frac{(1+a)^{b'\ell_B}}{\Gamma(1+b'\ell_B)} e^{-b'\ell_B \ln(E_o/\Delta)} \int_{E'+\Delta}^{E'_{max}(E_o')} dE'' \frac{d^2\sigma}{d\Omega dE''}(E_o,E'',\theta)_{TH} I_e(E'',E',\ell_A)$$

$$+ \int_{E'_{o_{min}}}^{E_o-\Delta} dE' \int_{E'+\Delta}^{E'_{max}(E_o')} dE'' I_e(E_o,E_o',\ell_B) \frac{d^2\sigma}{d\Omega dE''}(E_o',E'',\theta)_{TH} I_e(E'',E',\ell_A),$$

where

$$I_e(E_o,E',t) = \frac{(1+a)^{b't}}{E_o} \left(\frac{E'}{E_o}\right)^a \left(\frac{[\ln(E_o/E')]^{b't-1}}{\Gamma(b't)}\right)$$

is the Eyges[90] straggling function for which a and b' are functions of E'/E_o found by fitting the bremsstrahlung cross section for this straggling function to the bremsstrahlung cross section according to Bethe and Ashkin.[91]

$$\Delta = 0.001\ E_o/[1 + (2E_o/M)\sin\frac{2\theta}{2}]$$

$E'_{o_{min}}$ and $E'_{max}(E'_o)$ are the minimum E'_o and maximum E" kinematically permitted.

ℓ_A and ℓ_B were defined previously.

$\frac{d^2\sigma}{d\Omega dE'}(E_o,E',\theta)_{TH}$ is the cross section for quasi-elastic e-d scattering or is replaced by the elastic e-p or e-n scattering cross sections for the calculation of the elastic e-p and e-n radiative tails. Cross sections for quasi-elastic e-d scattering were from the method of Durand[52] using S- and D-state Hamada-Johnston wave functions.[48] The elastic cross sections were obtained from the Rosenbluth equation, assuming form-factor scaling.

The expression used in the inelastic radiative corrections is

$$\frac{d^2\sigma}{d\Omega dE'}(E_o,E',\theta) = C\{\frac{d^2\sigma}{d\Omega dE'}(E_o,E',\theta)_M - I_2^B - I_2^A\}$$

where

$\frac{d^2\sigma}{d\Omega dE'}(E,E',\theta)_M$ is the experimentally measured cross section after subtraction of elastic and quasi-elastic radiative tails;

$\frac{d^2\sigma}{d\Omega dE'}(E_o,E',0)$ is the radiatively corrected cross section;

$$C = [1 - (0.58 + a)\ (t_A + t_B)b]\exp\ (\delta_T + \delta_R)], \qquad \text{(A.II.4)}$$

$$\delta_T = bt_A\ \ln(E'/\Delta E') + bt_B\ \ln(E_o/\Delta E_o),$$

$$\delta_R = \frac{\alpha}{\pi}\{(28/9) - (13/6)\ln(q^2/m^2) + [\ln(q^2/m^2) - 1][\ln(E_o/\Delta E_o) + \ln(E'/\Delta E')]\}$$

ΔE_o = 1/2 a bin width in E_o,

$\Delta E'$ = 1/2 a bin width in E',

m = electron mass,

a = 0.25

and

I_2^B and I_2^A are integrals over the previously corrected data:

$$I_2^B = (1 + 0.58bL)(\Delta/E_o)^{b\ell_B}[1 + (1 - \Delta/E_o)ab\ell_B]$$

$$\cdot \int_{E' + \Delta E'}^{E'_{max}} dE_{of}[\ln(E_{of}/E')]^{b\ell_A}(E_{of} - E')^{-1}(bt_A R_A + v_A v' S_A) \qquad \text{(A.II.5)}$$

$$\cdot \frac{d^2\sigma}{d\Omega dE'}(E_o, E_{of}, \theta),$$

$$I_2^A = (1 + 0.58bL)\ (\Delta'/E')^{b\ell_A}[1 + (1 - \Delta'/E')ab\ell_A]$$

$$\cdot \int_{E_{o_{min}}}^{E_o - \Delta E_o} dE'_o[\ln(E_o/E'_o)]^{b\ell_B}(E_o - E'_o)^{-1}(bt_B R_B + v_B v' S_B) \qquad \text{(A.II.6)}$$

$$\cdot \frac{d^2\sigma}{d\Omega dE'}(E'_o, E', \theta)$$

where

$$L = t_A + t_B + (v_A + v_B)/b,$$

$$v_A = v_B = \frac{\alpha}{\pi}[\ln(q^2/m^2) - 1],$$

$$v' = 1 + 1/2(v_A + v_B)(1 + \ln(\eta))$$

$$\eta = 1 + (2E_o/M)\sin^2\frac{\theta}{2},$$

$$\Delta = 1/2[E_o - E'/(1 - (2E'/M)\sin^2\frac{\theta}{2})],$$

$$\Delta' = 1/2[E_o/(1 + (2E_o/M)\sin^2\frac{\theta}{2}) - E'],$$

$$R_A = E'/E_{of} + 3/4[(E_{of} - E')/E_{of}]^2,$$

$$R_B = E_o'/E_o + 3/4[(E_o - E_o')/E_o]^2,$$

$$S_A = E'/E_{of} + 1/2[(E_{of} - E')/E_{of}]^2,$$

$$S_B = E_o'/E_o + 1/2[(E_o - E_o')/E_o]^2,$$

and other terms have been defined previously.

The radiative corrections to the measured elastic cross sections used the formula:

$$C(\Delta E') = \{(1 + 1.103t_B)(1 + 1.103t_A)\} \exp[a_o+b_o+\delta(\Delta E')] \qquad (A.II.7)$$

where

$$a_o = (4/3)t_A \ \ell n(E_o/\eta\Delta E')$$

$$b_o = (4/3)t_B \ \ell n(E_o/\eta^2\Delta E')$$

$$\eta = 1 + \left(\frac{2E_o}{M}\right) \sin^2 \frac{\theta}{2}$$

and $\delta(\Delta E')$ is calculated following Tsai.[45] $\Delta E'$ is the width of the missing energy bin to which the correction factor $C(\Delta E')$ is applied to correct for electrons lost from that bin because of radiative energy loss.

APPENDIX III: NUCLEAR BINDING EFFECTS IN THE DEUTERON

Extraction of neutron differential cross-sections from e-d differential cross sections requires corrections for nuclear binding effects in the deuteron. In deep inelastic electron scattering processes, the most important corrections arise from the Fermi motion of the neutron and the proton.[20] In the following discussion we present an outline of the calculation of the Fermi motion effects, commonly referred to as "smearing" effects. The method used is derived from the work of Atwood and West.[19] Also discussed are other binding corrections which are expected to be small.

Investigations of deuteron binding corrections[19,20] primarily utilize the incoherent impulse approximation. In this approximation, as shown in Figure (42), only one nucleon is directly engaged in the scattering process (the interaction nucleon) while the other nucleon (the spectator nucleon) is unaffected. The spectator nucleon is on the mass shell before and after the interaction, while the interaction nucleon is initially off the mass shell and is brought back on to the mass shell by the absorption of the virtual photon. The square of the deuteron scattering matrix elements is then the sum of the squares of the corresponding neutron and proton matrix elements. An evaluation of the amplitude of the process in the diagram of Figure (42) will yield a relationship between

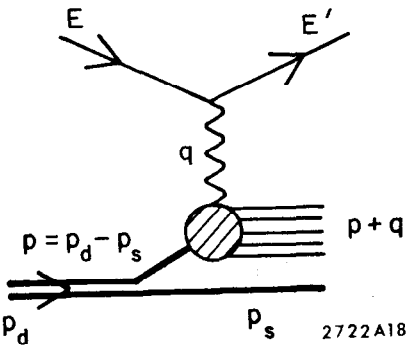

Fig. 42. Feynman diagram for inelastic electron-deuteron scattering.

deuteron and corresponding neutron and proton matrix elements. The deuteron electromagnetic tensor $W^d_{\mu\nu}$ is directly related to the square of the invariant matrix element for scattering from deuterium. Atwood and West[19] express the deuteron tensor in terms of off-shell neutron and proton tensors:

$$W^d_{\mu\nu} = \int_0^\infty |f(\vec{p})|^2 [W^p_{\mu\nu} + W^n_{\mu\nu}] d^3\vec{p} \qquad \text{(A.III.1)}$$

where

$$W^p_{\mu\nu} = -W^p_1(q^2, W'^2, q\cdot p)\left(q_{\mu\nu} - \frac{q_\mu q_\nu}{q^2}\right) + \frac{W_2(q^2, W'^2, q\cdot p)}{M^2}\left(p_\mu - \frac{q\cdot p}{q^2}q_\mu\right)\left(p_\nu - \frac{q\cdot p}{q^2}q_\nu\right) \qquad \text{(A.III.2)}$$

with an analogous expression for $W^n_{\mu\nu}$.

Here $p = p_d - p_s$ is the off-shell four momentum of the interacting nucleon, and p_s is the four-momentum of the on-shell spectator nucleon. The momentum p_d is the four-momentum of the target deuteron. We define the $\underline{3}$ direction to be the direction of the virtual-photon's momentum $q = (0,0,q_3,\nu)$ in the laboratory system. In the laboratory system we also have $p_d = (0,0,0,M_d)$ where M_d is the deuteron mass; and $p = (p_x,p_y,p_3,p_o) = (\vec{p},p_o) = (-\vec{p}_s,p_o)$ where $p_o = M_d - (p_s^2 + M^2)^{1/2}$. The square of the mass of the interacting nucleon's final state is $(W')^2 = (p+q)^2$.

The off-shell structure functions W_1 and W_2 in equation (A.III.2) depend on the three independent invariants $Q^2 = -q^2, (W')^2$, and $\nu' = q.p/M$ (defined such that all three are positive definite).

The three variables are independent because the interacting nucleon is off the mass shell and p^2 is variable.

The quantity $|f(\vec{p})|^2$ is the momentum distribution of the nucleon within the deuteron. By making a correspondence with elastic e-d scattering West[19] identifies $|f(\vec{p})|^2$ with the square of the non-relativistic deuteron wave function in momentum space $|\phi(\vec{p})|^2$. The quantity $|\phi(\vec{p})|^2$ is spherically symmetric and can be directly expressed in terms of the S-wave and D-wave components of the nonrelativistic deuteron wave function.

$$|f(\vec{p})|^2 = |\phi(|\vec{p}|)|^2 = |U_p(\vec{p})|^2 + |W_p(\vec{p})|^2 \equiv |f(|\vec{p}|)|^2 \qquad \text{(A.III.3)}$$

The S-wave component is

$$U_p(\vec{p}) = \left(\frac{1}{2\pi^2}\right)^{1/2} \int_o^\infty \frac{U(r)}{r} j_o(|\vec{p}|r) r^2 dr;$$

the D-wave component is

$$W_p(\vec{p}) = \left(\frac{1}{2\pi^2}\right)^{1/2} \int_o^\infty \frac{W(r)}{r} j_2(|\vec{p}|r) r^2 dr$$

The Hamada-Johnston wave function[48] was used in the calculation of smearing connections for these experiments.

The tensor equation (A.III.1) yields 16 separate dependent equations, one for each component. Examination of the various tensorial components yields the following two equations:

$$W_{1s}^p = \int_o^\infty |f(\vec{p})|^2 \left[W_1(Q^2, W'^2, \nu') + W_2(Q^2, W'^2, \nu') \frac{|\vec{p}|^2 - p_3^2}{2M^2}\right] d^3\vec{p}$$

(A.III.4)

$$W_{2s}^{p} = \int_{o}^{\infty} |f(\vec{p})|^2 [(1 - \frac{p_3 Q^2}{M\nu' q_3})^2 (\frac{\nu'}{\nu})^2 + \frac{|\vec{p}|^2 - p_3^2}{2M^2} (\frac{Q^2}{q_3^2})] W_2(Q^2, \nu', W'^2) d^3\vec{p}$$

where W_{1s}^{p} and W_{2s}^{p} are smeared proton structure functions. Similar expressions are obtained for the smeared neutron structure functions W_{1s}^{n} and W_{2s}^{n}. The deuteron structure functions are taken to be the sum of the corresponding smeared proton and neutron structure functions.

$$W_1^d(Q^2,\nu) = W_{1s}^{p}(Q^2,\nu) + W_{1s}^{n}(Q^2,\nu) \qquad \text{(A.III.5)}$$

$$W_2^d(Q^2,\nu) = W_{2s}^{p}(Q^2,\nu) + W_{2s}^{n}(Q^2,\nu)$$

We define the following "smearing ratios" of structure functions:

$$S_{p1} = W_1^p / W_{1s}^p, \quad S_{p2} = W_2^p / W_{2s}^p \qquad \text{(A.III.6)}$$

$$S_{n1} = W_1^n / W_{1s}^n, \quad S_{n2} = W_2^n / W_{2s}^n.$$

The smeared and unsmeared structure functions can be combined according to equation (I.1) to form smeared and unsmeared differential cross-sections ($\sigma_{ps}, \sigma_{ns}, \sigma_p, \sigma_n$). The smearing ratios (or smearing corrections) for the cross sections are defined in an analogous way:

$$S_p = \frac{\sigma_p}{\sigma_{ps}} \qquad S_n = \frac{\sigma_n}{\sigma_{ns}} \qquad \text{(A.III.7)}$$

and $U = S_n/S_p$ is defined as the unsmearing correction.

A.III.A. Identification of Off-Shell Structure Functions

The off-shell structure functions are identified[20] with the on-shell structure functions for the same Q^2 and $(W')^2 = W^2$. The Fermi motion does not change the effective Q^2 of the interaction because the four-momentum transfer is determined by the electron's kinematics and is independent of whether the initial nucleon is on or off the mass shell. However, conservation of energy requires that the effective W is dependent on the off-shell kinematics, as energy is required to bring the nucleon back on to the mass-shell. Some distinct features of the structure functions are directly dependent on the final state mass. For example, the distinction between quasielastic and inelastic electron-deuteron scattering is determined by whether the final state of the interacting nucleon is a single nucleon or contains pions. The off-shell structure functions must vanish at pion threshold ($W' = M + m_\pi$ where m_π is the pion mass). Also, the resonance spectra are described by functions of W for on-mass-shell structure functions. They should be described by the same functions of W' for off-shell structure functions if the resonance masses are to be the same. The off-shell structure functions were defined in terms of on-shell structure functions as follows:

$$W_1(Q^2,W'^2,\nu')\big|_{\text{off-shell}} \equiv W_1(Q^2,W'^2)\big|_{\text{off-shell}} \equiv W_1(Q^2,W^2)\big|_{\text{on-shell}}$$

(A.III.8)

$$W_2(Q^2,W'^2,\nu')\big|_{\text{off-shell}} \equiv W_2(Q^2,W'^2)\big|_{\text{off-shell}} \equiv W_2(Q^2,W^2)\big|_{\text{on-shell}}$$

In our analysis, according to the above definitions, the off-shell structure functions were described by the universal fit (given in section V.C, equation (V.1)), as follows:

$$W_2\big|_{\text{off-shell}} = \frac{A(W',Q^2)f(\tilde{\omega}_W)}{\tilde{\nu}\tilde{\omega}}$$

(A.III.9)

$$W_1\big|_{\text{off-shell}} = \left(\frac{1 + \tilde{\nu}^2/Q^2}{1 + R}\right) W_2\big|_{\text{off-shell}}$$

where $\tilde{\omega}_W = \frac{2M\tilde{\nu} + a^2}{Q^2 + b^2}$, $\tilde{\omega} = \frac{2M\tilde{\nu}}{Q^2}$, and $\tilde{\nu} = \frac{W' - Q^2 - M^2}{2M}$; for R,

we used $R_p = R_n = 0.18$.

These structure functions correspond to the case of no off-shell corrections.

In order to get some idea of possible off-shell corrections, the smearing expressions (eq. A.III.4) were investigated[20, 63] in the limit $Q^2 \to 0$, where the longitudinal virtual photoabsorption cross section for the deuteron, σ_{LD} must vanish according to gauge invariance. It has been shown[20, 63] that the smearing

expressions do not yield a vanishing σ_{LD} as $Q^2 \to 0$ unless small off-shell corrections are applied to the structure functions. As $Q^2 \to 0$, equation (A.III.4) become

$$W_1^d(Q^2,\nu) = \int |f(\vec{p})|^2 \{ W_1^p(Q^2,W') + W_1^n(Q^2,W') \} \, d^3\vec{p}$$

$$W_2^d(Q^2\nu) = \int |f(\vec{p})|^2 \left(\frac{\nu'}{\nu}\right)^2 \{ W_2^p(Q^2,W') + W_2^n(Q^2,W') \} \, d^3\vec{p} \qquad \text{(A.III.10)}$$

Now, from equation (I.3) in the limit $Q^2 \to 0$,

$$\sigma_{LD} = \frac{4\pi^2\alpha}{\nu} \{ \frac{\nu^2}{Q^2} W_2^d(\nu,Q^2) - W_1^d(\nu,Q^2) \} \qquad \text{(A.III.11)}$$

Combining equations (A.III.10) and (A.III.11) we get

$$\lim_{\substack{Q^2\to 0 \\ \nu \text{ fixed}}} \sigma_{LD} = \frac{4\pi^2\alpha}{\nu} \int |f(\vec{p})|^2 \{ \left[\frac{\nu'^2}{Q^2} W_2^p(Q^2,W') - W_1^p(Q^2,W')\right] + \left[\frac{\nu'^2}{Q^2} W_2^n(Q^2,W') - W_1^n(Q^2,W')\right] \} \, d^3\vec{p} \qquad \text{(A.III.12)}$$

The above expression does not yield a vanishing σ_{LD} as $Q^2 \to 0$ because the off-shell structure functions as defined by equation (A.III.9) do not vanish for that particular combination of off-shell variables. The necessary limiting behavior is

$$\lim_{\substack{Q^2\to 0 \\ \nu \text{ fixed}}} \sigma_{Lp} \alpha \left[\frac{\nu'^2}{Q^2} W_2^p(Q^2,\nu') - W_1^p(Q^2,\nu')\right] = 0 \qquad \text{(A.III.13a)}$$

or

$$\lim_{\substack{Q^2\to 0 \\ \nu \text{ fixed}}} \sigma_{Lp} \alpha \left[\frac{\tilde{\nu}^2}{Q^2} W_2^p(Q^2,W') - W_1^p(Q^2,W')\right] = 0 \qquad \text{(A.III.13b)}$$

So it appears that a simple correspondence between on-shell structure functions and off-shell structure functions does

not yield a physical result at $Q^2 = 0$. This defect can be corrected by the application of off-shell corrections. However, the W dependence of the off-shell structure functions must remain invariant in order to maintain the proper threshold and resonance positions. One method to accomplish this end is a mixed variable approach wherein we factor out the resonance and threshold behavior in the $A(W,Q^2)$ part of the fit to the structure functions, as was already done in equation (A.III.9). In the mixed variable approach the off-shell $A(W,Q^2)$ is then $A(W',Q^2)$ while $\tilde{\nu}$ is replaced by ν' in equation (A.III.9). The constraint at $Q^2 = 0$ is satisfied as implied by equation(A.III.13a). Another way to satisfy this constraint is to apply multiplicative off-shell corrections to the structure functions which will make σ_{LD} vanish at $Q^2 = 0$ by yielding equation (A.III.13b) in that limit. For example, we define two possible off-shell corrections.

Off-shell correction A.

$$W_2^p(Q^2,W',\nu')\big|_{\text{off-shell}} = \left(\frac{\tilde{\nu}}{\nu'}\right)^2 W_2^p(Q^2,W)\big|_{\text{on-shell}}$$

$$W_1^p(Q^2,W',\nu')\big|_{\text{off-shell}} = W_1^p(Q^2,W)\big|_{\text{on-shell}} \qquad \text{(A.III.14)}$$

Off-shell correction B.

$$W_2^p(Q^2,W',\nu')\big|_{\text{off-shell}} = W_2^p(Q^2,W)\big|_{\text{on-shell}}$$

$$W_1^p(Q^2,W',\nu')\big|_{\text{off-shell}} = \left(\frac{\nu'}{\tilde{\nu}}\right)^2 W_1^p(Q^2,W)\big|_{\text{on-shell}} \qquad \text{(A.III.15)}$$

Note that any definition which yields off-shell correction A or off-shell correction B, or a linear combination of them, will also work. The three off-shell corrections that were discussed (mixed variables (MX), A and B) vanish as $Q^2 \to \infty$ because in that limit $\tilde{\nu} \to \nu'$.

The nominal smearing ratios used in our analysis were the average between the ratios obtained from the calculation using no off-shell corrections (A.III.9) and the ratios obtained using the mixed variable approach. The error in the smearing ratio due to the uncertainties in the off-shell corrections was taken to be the difference between the nominal smearing ratio and the ratio obtained with no off-shell corrections. The uncertainties in the extracted σ_n/σ_p values due to uncertainties in the off-shell corrections are given in Table (X) along with the other errors. Values of the nominal smearing ratios for W_1 and W_2 for the neutron and proton are presented in Table (XXVII) for the kinematic points (x,Q^2) used in the extraction of R and the structure functions. Smearing ratios for various off-shell corrections are presented in Table (XXVIII) for representative values of (x,Q^2).

A.III.B. Deuteron Wave Functions

There are phenomenological non-relativistic wave functions[65,75] other than the Hamada-Johnston wave functions[48]

Table XXVII. Nominal smearing ratios

x	Q^2	S_{p1}	S_{p2}	S_{n1}	S_{n2}	x	Q^2	S_{p1}	S_{p2}	S_{n1}	S_{n2}
0.100	1.0	1.015	1.012	1.017	1.014	0.400	2.0	1.032	1.032	1.032	1.033
0.100	1.25	1.015	1.012	1.017	1.014	0.400	3.0	1.028	1.028	1.028	1.029
0.100	1.5	1.015	1.013	1.017	1.015	0.400	4.0	1.028	1.028	1.028	1.028
0.100	2.0	1.015	1.013	1.017	1.015	0.400	5.0	1.027	1.028	1.027	1.027
0.100	2.5	1.015	1.013	1.017	1.015	0.400	6.0	1.027	1.028	1.027	1.027
						0.400	7.0	1.028	1.028	1.027	1.027
0.150	1.0	1.016	1.013	1.018	1.015	0.400	8.0	1.028	1.028	1.027	1.027
0.150	1.25	1.016	1.013	1.018	1.015	0.400	9.0	1.028	1.028	0.027	1.027
0.150	1.5	1.016	1.014	1.018	1.016						
0.150	2.0	1.016	1.015	1.018	1.016	0.500	3.0	1.033	1.035	1.032	1.034
0.150	2.5	1.016	1.015	1.018	1.017	0.500	4.0	1.031	1.032	1.029	1.031
0.150	3.0	1.017	1.015	1.018	1.017	0.500	5.0	1.030	1.031	1.028	1.029
0.150	3.5	1.017	1.016	1.018	1.017	0.500	6.0	1.030	1.030	1.027	1.028
						0.500	7.0	1.029	1.030	1.026	1.027
0.200	1.0	1.019	1.016	1.021	1.018	0.500	8.0	1.029	1.029	1.026	1.026
0.200	1.25	1.018	1.016	1.020	1.018	0.500	10.0	1.028	1.029	1.025	1.025
0.200	1.5	1.018	1.016	1.020	1.018	0.500	12.0	1.028	1.028	1.024	1.024
0.200	2.0	1.018	1.016	1.020	1.018						
0.200	2.5	1.018	1.017	1.020	1.019	0.600	5.0	1.025	1.027	1.019	1.021
0.200	3.0	1.018	1.017	1.020	1.019	0.600	6.0	1.026	1.028	1.019	1.021
0.200	3.5	1.019	1.018	1.020	1.019	0.600	7.0	1.025	1.027	1.017	1.019
0.200	4.0	1.019	1.018	1.020	1.019	0.600	8.0	1.024	1.025	1.016	1.017
						0.600	10.0	1.022	1.023	1.013	1.014
0.250	1.0	1.024	1.022	1.026	1.024	0.600	12.0	1.020	1.020	1.010	1.011
0.250	1.25	1.021	1.019	1.023	1.021	0.600	14.0	1.019	1.020	1.009	1.010
0.250	1.5	1.021	1.019	1.022	1.021						
0.250	2.0	1.020	1.019	1.022	1.021	0.667	6.0	1.014	1.017	1.003	1.006
0.250	2.5	1.020	1.019	1.022	1.021	0.667	7.0	1.013	1.013	1.000	1.003
0.250	3.0	1.020	1.020	1.022	1.021	0.667	8.0	1.012	1.014	0.998	1.001
0.250	4.0	1.021	1.020	1.022	1.021	0.667	10.0	1.009	1.011	0.994	0.995
0.250	5.0	1.021	1.020	1.022	1.022	0.667	12.0	1.006	1.007	0.989	0.991
						0.667	14.0	1.003	1.004	0.986	0.987
0.333	1.5	1.029	1.028	1.030	1.029	0.667	16.0	1.001	1.002	0.983	0.984
0.333	2.0	1.025	1.025	1.026	1.026						
0.333	2.5	1.025	1.024	1.026	1.025	0.750	8.0	0.968	0.971	0.943	0.947
0.333	3.0	1.025	1.024	1.025	1.025	0.750	9.0	0.973	0.976	0.946	0.950
0.333	4.0	1.025	1.024	1.025	1.025	0.750	10.0	0.968	0.970	0.939	0.942
0.333	5.0	1.025	1.025	1.025	1.025	0.750	12.0	0.965	0.967	0.933	0.936
0.333	6.0	1.025	1.025	1.025	1.025	0.750	14.0	0.960	0.962	0.926	0.929
0.333	7.0	1.025	1.025	1.025	1.025	0.750	16.0	0.955	0.957	0.920	0.922
						0.800	12.0	0.915	0.918	0.871	0.874
						0.800	14.0	0.906	0.909	0.858	0.862
						0.800	16.0	0.900	0.903	0.850	0.853

Table XXVIII. Smearing ratios for off-shell corrections

		No off-shell corr.		Various off-shell corrections						Various wave functions			
x	Q^2	SP_1^0 (HJ)	SP_2^0 (HJ)	SP_1^{MX} (HJ)	SP_2^{MX} (HJ)	SP_1^A (HJ)	SP_2^A (HJ)	SP_1^B (HJ)	SP_2^B (HJ)	SP_2^0 (RSC)	SP_2^0 (RHC)	SP_2^0 (FL)	SP_2^0 (HHC)
0.100	1.0	1.017	1.009	1.013	1.014	1.017	1.019	1.007	1.009	1.008	1.010	1.011	1.007
	1.5	1.016	1.011	1.014	1.014	1.016	1.017	1.010	1.011	1.009	1.012	1.013	1.008
	2.5	1.016	1.013	1.014	1.015	1.016	1.017	1.012	1.013	1.011	1.014	1.014	1.010
0.150	1.0	1.019	1.009	1.014	1.017	1.019	1.023	1.005	1.009	1.008	1.010	1.011	1.007
	2.0	1.018	1.013	1.015	1.016	1.018	1.020	1.011	1.013	1.011	1.014	1.014	1.009
	3.5	1.018	1.015	1.016	1.016	1.018	1.019	1.014	1.015	1.013	1.016	1.016	1.011
0.200	1.0	1.022	1.012	1.016	1.020	1.022	1.028	1.004	1.012	1.010	1.012	1.014	1.008
	2.5	1.020	1.016	1.016	1.018	1.020	1.022	1.013	1.016	1.013	1.016	1.017	1.011
	4.0	1.020	1.017	1.017	1.019	1.020	1.021	1.016	1.017	1.015	1.018	1.018	1.013
0.250	1.0	1.027	1.017	1.021	1.027	1.028	1.037	1.006	1.017	1.014	1.018	1.019	1.013
	3.0	1.023	1.019	1.018	1.021	1.023	1.025	1.016	1.019	1.014	1.019	1.020	1.014
	5.0	1.023	1.020	1.020	1.021	1.023	1.024	1.018	1.020	1.018	1.021	1.021	1.015
0.333	1.5	1.033	1.026	1.025	1.031	1.033	1.042	1.015	1.026	1.023	1.026	1.027	1.020
	4.0	1.027	1.024	1.022	1.025	1.027	1.031	1.021	1.024	1.021	1.025	1.025	1.018
	7.0	1.027	1.025	1.023	1.025	1.027	1.029	1.023	1.025	1.022	1.026	1.025	1.019
0.400	2.0	1.036	1.031	1.027	1.033	1.037	1.046	1.021	1.031	1.028	1.032	1.032	1.024
	5.0	1.031	1.028	1.024	1.027	1.031	1.034	1.024	1.028	1.026	1.029	1.028	1.022
	9.0	1.030	1.028	1.026	1.027	1.030	1.032	1.026	1.028	1.026	1.029	1.028	1.022
0.500	3.0	1.040	1.036	1.027	1.034	1.040	1.048	1.027	1.036	1.033	1.037	1.037	1.029
	7.0	1.033	1.031	1.025	1.028	1.033	1.037	1.028	1.031	1.029	1.032	1.031	1.026
	12.0	1.030	1.029	1.025	1.027	1.030	1.033	1.027	1.029	1.027	1.030	1.029	1.025
0.600	5.0	1.033	1.031	1.018	1.024	1.033	1.040	1.023	1.031	1.029	1.032	1.031	1.026
	8.0	1.029	1.028	1.018	1.022	1.029	1.034	1.023	1.028	1.027	1.029	1.029	1.025
	14.0	1.022	1.022	1.015	1.018	1.022	1.025	1.019	1.022	1.021	1.022	1.023	1.020
0.667	6.0	1.023	1.022	1.005	1.012	1.023	1.031	1.014	1.022	1.021	1.023	1.023	1.019
	10.0	1.015	1.015	1.002	1.007	1.016	1.020	1.010	1.015	1.014	1.015	1.016	1.014
	16.0	1.006	1.005	0.996	0.999	1.006	1.009	1.002	1.005	1.005	1.005	1.007	1.007
0.750	8.0	0.978	0.978	0.957	0.964	0.979	0.986	0.970	0.978	0.979	0.973	0.981	0.981
	12.0	0.973	0.973	0.956	0.961	0.974	0.979	0.967	0.973	0.975	0.973	0.977	0.980
	16.0	0.962	0.962	0.948	0.952	0.962	0.967	0.958	0.962	0.964	0.961	0.967	0.971
0.800	12.0	0.926	0.926	0.903	0.910	0.926	0.933	0.919	0.926	0.929	0.925	0.932	0.938
	14.0	0.917	0.917	0.896	0.902	0.917	0.923	0.910	0.917	0.921	0.915	0.923	0.930

which can also be used. These wave functions should describe all known properties of the deuteron such as its binding energy, magnetic and quadrupole moment, the n-p phase shifts and the measured elastic e-d form factors.[49] The elastic e-d measurements[49] indicate that the Hamada-Johnston wave function[48] (HJ) and the Reid soft-core (RSC) and hard-core (RHC) wave functions[65] are in best agreement with the measured form factors. The Feshbach-Lomon (FL) and the Hulthén hard core (HHC) wave functions are in lesser agreement with the measured form factors. The Hulthén (no core) wave function is in poor agreement with those measurements. The momentum distributions obtained from some of these wave functions are shown in Figure (43). The smearing ratios calculated using these wave functions are presented for comparison in Table (XXVIII).

A.III.C. Effects of Smearing on R

As is evident from Table (XXVII), the smearing corrections for W_1 and W_2 are nearly the same, i.e., $S_{p1} \cong S_{p2}$ and $S_{n1} \cong S_{n2}$. A straightforward derivation[20] shows that in that case the smeared and unsmeared values of R are equal and R_n can be directly extracted from the measured hydrogen and deuterium data by the following expression:

$$R_d = R_p\left(\frac{1}{1+Z}\right) + R_n\left(\frac{Z}{1+Z}\right) \qquad \text{(A.III.16)}$$

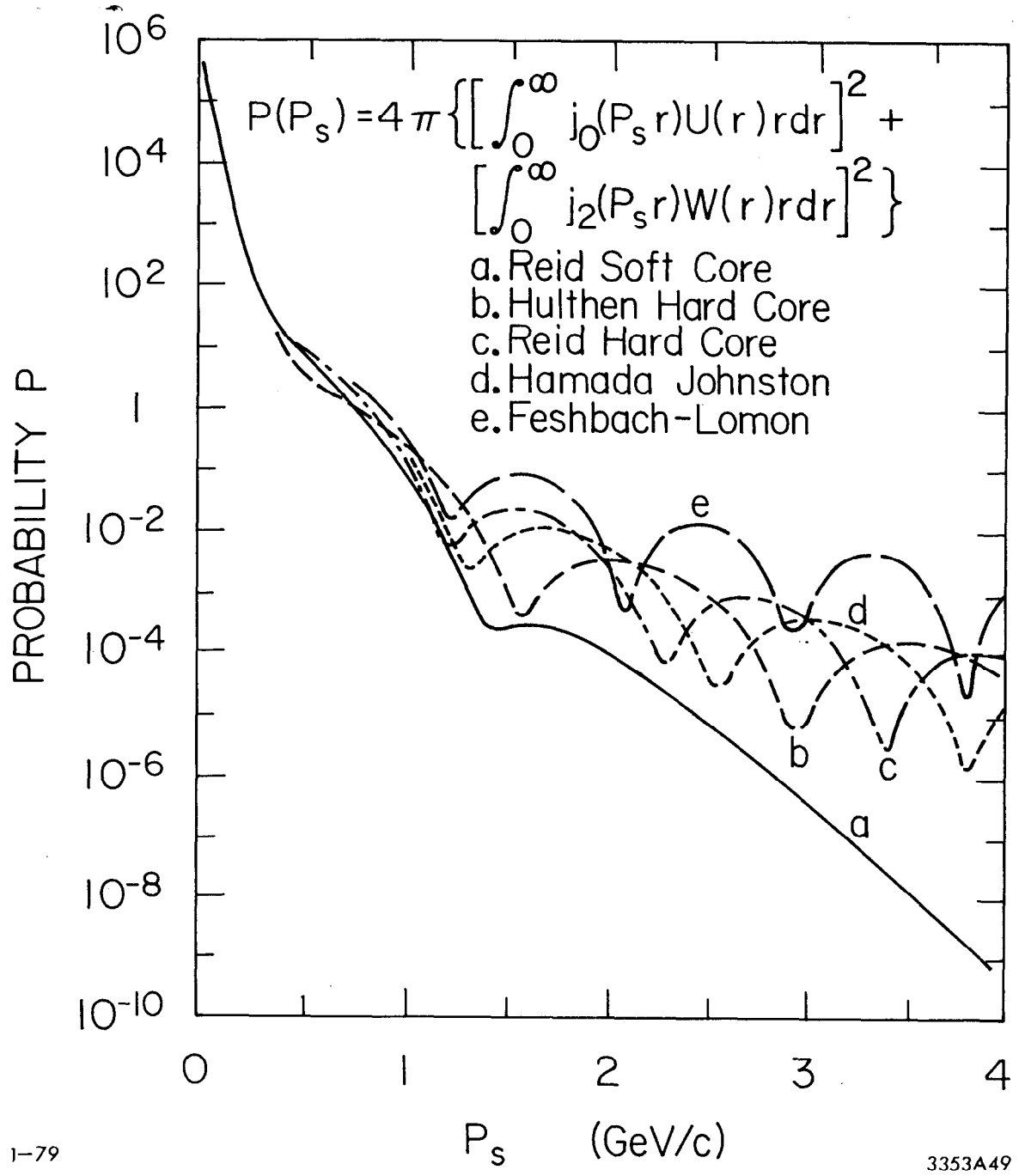

Fig. 43. Momentum distributions in the deuteron for five different wave functions.

or

$$R_n = R_d + \frac{\delta}{Z} \qquad \text{(A.III.17)}$$

where $\delta = R_d - R_p$ and $Z = W_{1s}^n / W_{1s}^p = (W_1^n / W_1^p)(S_{n1}/S_{p1})$ is the smeared neutron to proton ratio for the W structure function. The above expression implies that if we find that $R_d = R_p$ (i.e., $\delta = 0$) then it follows that $R_n = R_p$. It also follows that the uncertainty in the extracted R_n is largest at small ω because in that region the neutron to proton ratio is small.

On the other hand if $S_{p1} \neq S_{p2}$ then smearing affects R and the smeared value of $R_p (R_{ps})$ will not be equal to R_p. As was discussed in section (A.III.A), possible off-shell corrections to the structure functions could be different for W_1 and W_2 and yield values of S_{p1} which are different from S_{p2}. The difference between the smeared and unsmeared values of R_p is then

$$\gamma_p = R_{ps} - R_p = \left(\frac{S_{p1}}{S_{p2}} - 1\right)(1 + R_p) \qquad \text{(A.III.18)}$$

and

$$R_d = R_{ps}\left(\frac{1}{1 + Z}\right) + R_{ns}\left(\frac{Z}{1 + Z}\right) \qquad \text{(A.III.19)}$$

Representative values of γ_p, calculated using our fit to the proton data under the assumption $R_p = 0.18$, are given in Table (XXIX) along with various possible off-shell corrections. These values can be taken as the estimate of the possible changes in R_p due to off-shell effects in the deuteron. Uncertainties

Table XXIX. Typical values of γ_p

x	Q^2	γ_p^{nom}	γ_p^0	γ_p^{MX}	γ_p^A	γ_p^B
0.100	1.0	0.004	0.009	-0.002	-0.002	-0.003
	1.5	0.003	0.006	-0.001	-0.001	-0.002
	2.5	0.002	0.004	-0.001	-0.001	-0.001
0.150	1.0	0.004	0.011	-0.003	-0.004	-0.005
	2.0	0.002	0.006	-0.002	-0.002	-0.002
	3.5	0.001	0.003	-0.001	-0.001	-0.001
0.200	1.0	0.004	0.012	-0.005	-0.007	-0.009
	2.5	0.002	0.005	-0.002	-0.003	-0.003
	4.0	0.001	0.003	-0.001	-0.002	-0.002
0.250	1.0	0.003	0.012	-0.006	-0.010	-0.013
	3.0	0.001	0.005	-0.003	-0.003	-0.003
	5.0	0.001	0.003	-0.002	-0.002	-0.002
0.330	1.5	0.001	0.008	-0.007	-0.010	-0.012
	4.0	0.001	0.004	-0.003	-0.004	-0.004
	7.0	0.000	0.002	-0.002	-0.002	-0.002
0.400	2.0	-0.001	0.006	-0.007	-0.010	-0.011
	5.0	-0.001	0.003	-0.004	-0.004	-0.004
	9.0	0.000	0.002	-0.002	-0.002	-0.002
0.500	3.0	-0.001	0.004	-0.007	-0.010	-0.010
	7.0	-0.001	0.002	-0.004	-0.004	-0.004
	12.0	-0.001	0.001	-0.002	-0.002	-0.003
0.600	5.0	-0.003	0.002	-0.007	-0.008	-0.009
	8.0	-0.002	0.001	-0.005	-0.005	-0.005
	14.0	0.001	0.001	-0.003	-0.003	-0.003
0.667	6.0	-0.004	0.001	-0.008	-0.008	-0.009
	10.0	-0.002	0.001	-0.005	-0.005	-0.006
	16.0	0.002	0.001	-0.004	-0.004	-0.004
0.750	8.0	-0.005	0.000	-0.009	-0.009	-0.009
	12.0	-0.004	0.000	-0.007	-0.007	-0.007
	16.0	-0.003	0.000	-0.005	-0.005	-0.005
0.800	12.0	-0.005	0.000	-0.009	-0.008	-0.009
	14.0	-0.004	0.000	-0.008	-0.008	-0.008
	16.0	-0.004	0.000	-0.007	-0.007	-0.007

in the wave function do not affect R because they influence W_1 and W_2 in the same way.

A.III.D. Other Deuteron Corrections

Other deuteron corrections which were neglected in our incoherent impulse approximation are the subject of this section. The incoherent impulse approximation is expected to work best at large values of Q^2. Most corrections to the impulse approximation are expected to be small in the Q^2 range of this experiment (1 to 20 GeV^2). Similar discussions of corrections to the impulse approximation in the case of inelastic e-d scattering are given in references (19) and (20).

1. Glauber type[92] shadowing corrections. This is a multiple scattering correction which occurs because one nucleon may shadow the other. It is important in hadronic scattering where cross sections are large. In hadronic reactions this correction is typically[19] 5% even at asymptotic energies. In electron scattering the double scattering is presumably electromagnetic and therefore suppressed[19] by a factor of α. Calculations[20] show that in that case the correction is less that 0.1% at an incident electron energy of 20 GeV. The vector dominance[13, 93] allows a virtual photon to propagate as a hadron such that the second scattering is hadronic and therefore not suppressed. However, simple vector dominance models[13, 94] also predict large shadowing in

electron scattering from high A nuclei. These predictions are in disagreement with experiment.[93] Experimentally, no shadowing was observed in the electroproduction experiment even at Q^2 values as low as 0.25 GeV^2. These experiments indicate that shadowing will also be small in the deuteron. Further refinements[95] of the vector dominance model yield shadowing corrections for high A nuclei markedly smaller than those of the old vector dominance model. The new theories predict little shadowing at high Q^2 and small ν. Therefore, even within vector dominance theories the shadowing correction in deuterium is expected to be small in the Q^2 range of this experiment.

2. Interference terms and coherent effects. These corrections have been estimated[20] to be on the order of $F_d^2(Q^2)$, the square of the wave function part of the deuteron form factor, which is negligible in the Q^2 range of this experiment.

3. Meson currents in the deuteron. These corrections arise from the fact that the deuteron wave function probably contains a small amplitude for the deuteron to exist as two nucleons and one or more pions, a nucleon and a nucleon isobar state and other such states. These corrections are known to be small in elastic e-d scattering [50], and in quasielastic e-d scattering[96], and probably contribute only at large ω.

4. Off-mass-shell corrections to the nucleon structure

functions. Some estimates of these corrections have been made in this appendix. The error arising from uncertainties in these corrections has been included in our final errors.

5. Final state interaction effects. These effects are known to be small at large Q^2 for quasielastic e-d scattering.[50,52,97,98] These effects are only important when the relative momentum between the outgoing final particles is small. In the deep inelastic case, these effects are expected to be small[20] because of the large energy and momentum transfers that are involved.

6. Relativistic corrections to the deuteron wave function. The practical relativistic bound state problem is still in a rather crude state. It is possible that the phenomenological non-relativistic deuteron wave functions that we use may include relativistic effects in a phenomenological way because they are fitted to data. There have also been suggestions[19] that the deuteron wave function contains high momentum components in larger than expected amounts. The existence of a large amplitude for high momentum means that if those high-momentum wave functions were used in the extraction of σ_n from present deuterium data then σ_n would be smaller than the cross section extracted with standard deuteron wave functions. The extracted neutron cross section is small in the small ω region; therefore, the inclusion of a large amplitude for high momentum

components will result in a neutron cross section which is extremely small (i.e., $\sigma_n/\delta_p \gtrsim 0$) or even negative. There is no convincing evidence at present for the existence of a large amplitude for high momentum components in the deuteron wave function. Experiments in which the spectator momentum distribution in deuteron quasielastic hadronic processes is measured[99] can account for the observed distribution within models based on conventional wave functions and including Glauber and final state corrections.

Recently, theoretical studies[100,101] of the deuteron wave function in the infinite momentum frame have indicated that relativistic corrections may decrease the smearing ratio $S_p = \sigma_p/\sigma_{ps}$ by a small fraction which varies from 1.5% at $x = 0$ to 3% at $x = 0.8$. These corrections are such as to <u>decrease</u> the final extracted neutron cross section over the entire range of x, and bring the ratio σ_n/σ_p down closer to the quark model limit of 0.25.